bridge. The bridge consists of a polarization beamsplitter oriented at 45° to the incident laser polarization, and θ_F is measured via the normalized intensity difference between the two orthogonal components at ±45°: $2\theta_F \cong (I_{+45} - I_{-45})/(I_{+45} + I_{-45})$. The photodiode difference current is converted to voltage (transimpedance gain = 40 V mA^{-1}, or ~20 V per mW of unbalanced laser power at 790 nm) and measured in a spectrum analyser. Above a few kilohertz, the measured noise floor arises primarily from photon shot noise, which contributes ~175 nV Hz$^{-1/2}$ of spectrally flat (white) noise at a typical laser power of 200 μW. The photodiodes and amplifier contribute an additional 65 nV Hz$^{-1/2}$ of uncorrelated white noise. All noise spectral densities are r.m.s. values, and spectra were typically signal-averaged for 10–20 min. The accuracy of measured hyperfine constants and *g*-factors was imposed by the ±0.01 G resolution of the Hall bar magnetic field sensor. Measurement of inter-hyperfine spin coherence (Fig. 4d) was performed with a higher-bandwidth, lower gain amplifier (~0.70 V mA^{-1}), and a typical laser power of 3.5 mW. Unless otherwise stated, measurements of rubidium (potassium) vapour were performed with 250 (125) torr of nitrogen buffer gas, which broadens the linewidth of the D1 and D2 optical transitions and causes the motion of the alkali atoms to become diffusive (thereby increasing the average time the atoms spend in the laser beam and narrowing the magnetic resonance peaks.) The diameter of the laser beam in the vapour cell can be increased (decreased) by closing (opening) the aperture in front of the final focusing lens.

Received 12 May; accepted 2 July 2004; doi:10.1038/nature02804.

1. Johnson, J. B. Thermal agitation of electricity in conductors. *Nature* **119,** 50–51 (1927).
2. White, D. R. *et al.* The status of Johnson noise thermometry. *Metrologia* **33,** 325–335 (1996).
3. Itano, W. M. *et al.* Quantum projection noise: Population fluctuations in two-level systems. *Phys. Rev. A* **47,** 3554–3570 (1993).
4. Sorensen, J. L., Hald, J. & Polzik, E. S. Quantum noise of an atomic spin polarization measurement. *Phys. Rev. Lett.* **80,** 3487–3490 (1998).
5. Bloch, F. Nuclear induction. *Phys. Rev.* **70,** 460–474 (1946).
6. Sleator, T., Hahn, E. L., Hilbert, C. & Clarke, J. Nuclear-spin noise. *Phys. Rev. Lett.* **55,** 1742–1745 (1985).
7. Happer, W. & Mathur, B. S. Off-resonant light as a probe of optically-pumped alkali vapors. *Phys. Rev. Lett.* **18,** 577–580 (1967).
8. Suter, D. & Mlynek, J. Laser excitation and detection of magnetic resonance. *Adv. Magn. Opt. Res.* **16,** 1–83 (1991).
9. Kubo, R. The fluctuation-dissipation theorem. *Rep. Prog. Phys.* **29,** 255–284 (1966).
10. Weissman, M. B. What is a spin glass? A glimpse via mesoscopic noise. *Rev. Mod. Phys.* **65,** 829–839 (1993).
11. Smith, N. & Arnett, P. White-noise magnetization fluctuations in magnetoresistive heads. *Appl. Phys. Lett.* **78,** 1448–1450 (2001).
12. Awschalom, D. D., DiVincenzo, D. P. & Smyth, J. F. Macroscopic quantum effects in nanometer-scale magnets. *Science* **258,** 414–421 (1992).
13. Aleksandrov, E. B. & Zapassky, V. S. Magnetic resonance in the Faraday-rotation noise spectrum. *Zh. Eksp. Teor. Fiz.* **81,** 132–138 (1981).
14. Mitsui, T. Spontaneous noise spectroscopy of an atomic resonance. *Phys. Rev. Lett.* **84,** 5292–5295 (2000).
15. Kuzmich, A. *et al.* Quantum nondemolition measurements of collective atomic spin. *Phys. Rev. A* **60,** 2346–2350 (1999).
16. Kuzmich, A., Mandel, L. & Bigelow, N. P. Generation of spin squeezing via continuous quantum nondemolition measurement. *Phys. Rev. Lett.* **85,** 1594–1597 (2000).
17. Mamin, H. J., Budakian, R., Chui, B. W. & Rugar, D. Detection and manipulation of statistical polarization in small spin ensembles. *Phys. Rev. Lett.* **91,** 207604 (2003).
18. Manassen, Y., Hamers, R. J., Demuth, J. E. & Castellano, A. J. Direct observation of the precession of individual paramagnetic spins on oxidized silicon surfaces. *Phys. Rev. Lett.* **62,** 2531–2534 (1989).
19. Nussinov, Z., Crommie, M. F. & Balatsky, A. V. Noise spectroscopy of a single spin with spin-polarized STM. *Phys. Rev. B* **68,** 085402 (2003).
20. Cleland, A. N. & Roukes, M. L. Noise processes in nanomechanical resonators. *J. Appl. Phys.* **92,** 2758–2769 (2002).
21. Weaver, R. L. & Lobkis, O. I. Ultrasonics without a source: Thermal fluctuation correlations at MHz frequencies. *Phys. Rev. Lett.* **87,** 134301 (2001).
22. Kastler, A. Optical methods for studying Hertzian resonances. *Science* **158,** 214–221 (1967).
23. Happer, W. Optical pumping. *Rev. Mod. Phys.* **44,** 169–249 (1972).
24. Corney, A. *Atomic and Laser Spectroscopy* (Clarendon, Oxford, 1977).
25. Yabuzaki, T., Mitsui, T. & Tanaka, U. New type of high-resolution spectroscopy with a diode laser. *Phys. Rev. Lett.* **67,** 2453–2456 (1991).
26. Ito, T., Shimomura, N. & Yabuzaki, T. Noise spectroscopy of K atoms with a diode laser. *J. Phys. Soc. Jpn* **72,** 962–963 (2003).
27. Jury, J. C., Klaassen, K. B., van Peppen, J. & Wang, S. X. Measurement and analysis of noise sources in magnetoresistive sensors up to 6 GHz. *IEEE Trans. Magn.* **38,** 3545–3555 (2002).
28. Wolf, S. A. *et al.* Spintronics: A spin-based electronics vision for the future. *Science* **294,** 1488–1495 (2001).
29. Imamoglu, A. *et al.* Quantum information processing using quantum dot spins and cavity QED. *Phys. Rev. Lett.* **83,** 4204–4207 (1999).
30. Joglekar, Y. N., Balatsky, A. V. & MacDonald, A. H. Noise spectroscopy and interlayer phase coherence in bilayer quantum Hall systems. *Phys. Rev. Lett.* **92,** 086803 (2004).

Supplementary Information accompanies the paper on **www.nature.com/nature**.

Acknowledgements We thank P. Littlewood, S. Gider, P. Crowell and P. Crooker for discussions. This work was supported by the Los Alamos LDRD programme.

Competing interests statement The authors declare that they have no competing financial interests.

Correspondence and requests for materials should be addressed to S.A.C. (crooker@lanl.gov).

Negative intrinsic resistivity of an individual domain wall in epitaxial (Ga,Mn)As microdevices

H. X. Tang[1], S. Masmanidis[1], R. K. Kawakami[2], D. D. Awschalom[2] & M. L. Roukes[1]

[1]*Condensed Matter Physics 114-36, California Institute of Technology, Pasadena, California 91125, USA*
[2]*Department of Physics, University of California, Santa Barbara, California 93106, USA*

Magnetic domains, and the boundaries that separate them (domain walls, DWs), play a central role in the science of magnetism[1]. Understanding and controlling domains is important for many technological applications in spintronics, and may lead to new devices[2]. Although theoretical efforts have elucidated several mechanisms underlying the resistance of a single DW[3–8], various experiments[9–15] report conflicting results, even for the overall sign of the DW resistance. The question of whether an individual DW gives rise to an increase or decrease of the resistance therefore remains open. Here we report an approach to DW studies in a class of ferromagnetic semiconductors (as opposed to metals[16,17]) that offer promise for spintronics[18]. These experiments involve microdevices patterned from monocrystalline (Ga,Mn)As epitaxial layers. The giant planar Hall effect that we previously observed[19] in this material enables direct, real-time observation of the propagation of an individual magnetic DW along multiprobe devices. We apply steady and pulsed magnetic fields, to trap and carefully position an individual DW within each separate device studied. This protocol reproducibly enables high-resolution magnetoresistance measurements across an individual wall. We consistently observe negative intrinsic DW resistance that scales with channel width. This appears to originate from sizeable quantum corrections to the magnetoresistance.

Multiterminal devices for this work are patterned from $Ga_{0.948}Mn_{0.052}As$ epitaxial layers (epilayers; see Methods). The longitudinal device axis, along which the current flows, is oriented collinear with a cleave edge [110], also a cubic hard axis. Figure 1a displays the measurement set-up, showing utilization of three pairs of transverse (Hall) voltage probes to sense the magnetoresistance to the longitudinal current within the device (Methods).

(Ga,Mn)As films are intrinsically magnetized in-plane owing to a combination of compressive lattice-mismatch-induced strain and demagnetization effects[20]. The vector plot in Fig. 1b (inset) depicts the four in-plane easy axes. A representative *R*–*H* loop (here *R* is the giant planar Hall resistance[19], and *H* is magnetic field) is shown in Fig. 1b. At high negative field values the sample magnetization is saturated along easy axis I (Fig. 1b, inset). When the field is ramped up, the first jump corresponds to a magnetization transition from I to II (or [0$\bar{1}$0] to [100]); the second jump completes the reversal by switching from II to III (or [100] to [010]). The magnetization transitions evolve via the formation of a 90°-DW[19,21,22]. The square hysteresis loops obtained at low temperatures are indicative of magnetization switching dominated by wall propagation, rather than domain nucleation[2].

DW propagation experiments are carried out by inducing a free wall within the sample (Methods). Figure 1c shows the temporal evolution of signals obtained simultaneously using the sample's three transverse probes. The data are recorded with a drive field at point A in Fig. 1b (74 Oe). The successive jumps in the resistance versus time record for each of the three channels correspond to a single DW sequentially passing the transverse probe pairs. These

three resistance jumps display identical magnitudes and rise times, and DW propagation between adjacent pairs of voltage probes exhibits identical time intervals. Equal time delays are, in fact, expected as all probe-to-probe spacings are equal (100 μm for this measurement). These data are consistent with the picture that the DW retains a fixed shape while propagating along the device, with a speed that can be calculated directly from the time-of-flight between the probes. Detailed investigations we report elsewhere[23] demonstrate that DW velocity spanning four decades can be observed by varying the strength of the applied in-plane magnetic field. Two regimes—manifesting slow and fast dynamics, involving thermally assisted flow for low fields and viscous flow for high fields, respectively—have been identified[23].

Our initial domain wall resistance (DWR) measurements have been carried out quasistatically. First, an in-plane 'driving' field is adjusted so that a solitary DW propagates very slowly across the sample (~50 s delay between successive probes). Then, during the DW's traverse, we obtain high-resolution measurements of two distinct longitudinal resistances, which we term R^U_{xx} and R^D_{xx}, by lock-in detection with short, 30 ms, integration times. These involve either a pair of voltage probes on the top side of the device, $R^U_{xx} = R_{15,24}$, or a pair on the bottom, $R^D_{xx} = R_{15,86}$. (Here, conventional four-probe notation is used, with $R_{ij,kl}$ corresponding to a sensing current imposed from terminal i to j, which results in an induced potential from k to l.) Simultaneously, we also measure the transverse resistances obtained from the left and right transverse probes ($R^L_{xy} = R_{15,28}$, $R^R_{xy} = R_{15,46}$) that provide continuous monitoring of the arrival and departure of individual DWs from the 'measurement region' between probes (Fig. 2a).

Figure 2b displays the change in longitudinal resistance resulting from entrapment of a single DW within the measurement region. A perturbation as large as 0.6% (~30 Ω) is manifested; however, this rather conspicuous excess resistance cannot be interpreted as the intrinsic contribution from an individual DW, because both R^U_{xx} and R^D_{xx} comprise admixtures of both the longitudinal and planar Hall resistances. A sum rule holds: the difference between R^U_{xx} and R^D_{xx} equals that between transverse resistances R^L_{xy} and R^R_{xy} (Fig. 2c). Elsewhere[24], we describe a theoretical model for anisotropic

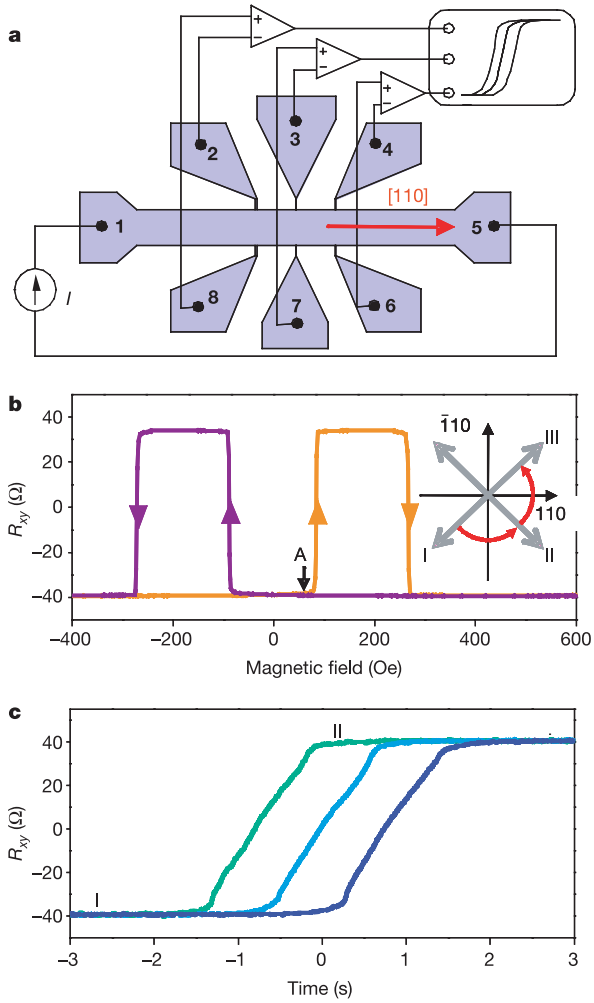

Figure 1 Sample configuration and measurement scheme. **a**, A constant sensing current is imposed between contacts 1 and 5, which are oriented along [110]. An external, in-plane magnetic field is applied 15° away from this axis. High-input-impedance differential amplifiers are used to make potential measurements across three transverse probes. **b**, A typical (transverse) giant planar Hall resistance, R_{xy}, versus magnetic field, H, hysteresis loop for a 100-μm-wide Hall bar at $T = 4.2$ K. Inset, schematic displaying orientation of the four in-plane easy axes of (Ga,Mn)As epilayers. **c**, After nucleation at one side of the sample, with a 74 Oe in-plane field applied, the DW propagates sequentially across the three transverse probes (differentiated by the coloured traces), successively generating transverse voltage signals.

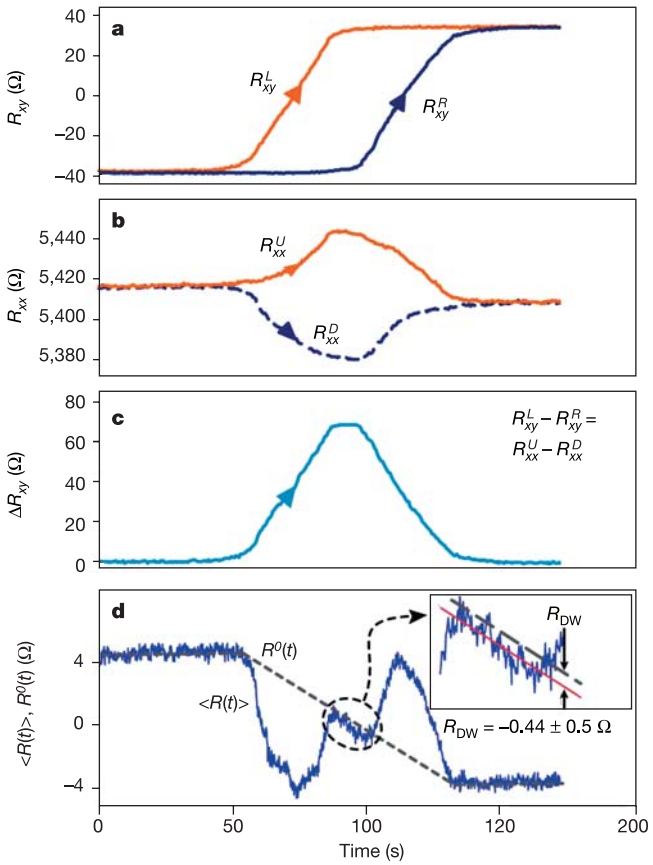

Figure 2 Time-resolved magnetoresistance measured across a single DW. **a**, Transverse resistance, R_{xy}, at 4.2 K from two pairs of probes monitoring the entrance and exit of a single DW from the channel. **b**, Longitudinal resistance, R_{xx}, across the wall is measured simultaneously from both the top and bottom of the device channel, R^U_{xx} and R^D_{xx} respectively. **c**, A resistance sum rule is satisfied: the difference between transverse resistances, $R^L_{xy} - R^R_{xy}$, is equal to the difference between longitudinal resistances $R^U_{xx} - R^D_{xx}$. **d**, When the DW is completely resident between probes, the difference between measured longitudinal resistance, $\langle R(t) \rangle$ (violet), and a simple model described in the text, $R^0(t)$ (dashed grey) allows differentiation of the predominant, eddy-like part of domain-induced magnetoresistance from the 'intrinsic' DWR.

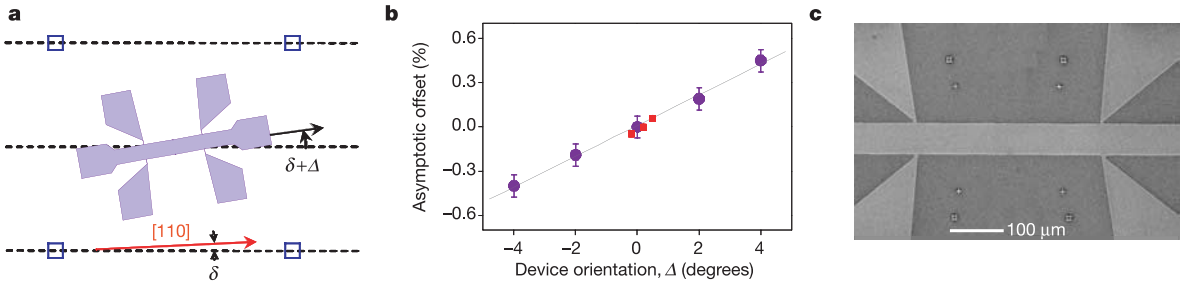

Figure 3 Scheme to align devices along the crystallographic [110] orientation. **a**, Arrays of alignment marks are patterned across a wafer with orientation along the natural 'cleave' axis. These are inadvertently misaligned an angle δ from the true [110] orientation. Subsequently, a series of devices are fabricated with angles stepped at 2° with respect to these alignment marks (for example, $\Delta = 0, \pm 2°, \pm 4°, \ldots$) The zero-field asymptotic magnetoresistance between magnetization states I and II are measured for each device and the one yielding the smallest value is identified; data are shown in **b**. For the next round, we fabricate another set of devices, on the same wafer using the same set of alignment marks, with orientation now stepped at 0.2° and centred about the optimal device identified in the first round. This process is iterated until devices with minimal offset are obtained for high-resolution investigations of DWR. Alignment accuracies of ~0.03° are realized. Data of Fig. 4 were obtained with devices oriented about $\delta \approx 0.10$–$0.13°$, which provided the closest alignment to [110]. Error bars represent standard error of the mean. **c**, Magnified view of a 60-μm-wide device, showing the region between two transverse probes.

('classical') Boltzmann transport across an individual DW. The model demonstrates that the experimentally observed longitudinal resistance perturbation can largely be attributed to the discontinuity in resistivity across a DW[24].

We wish to separate phenomena arising solely from the resistivity discontinuity at a DW from the more subtle magnetic scattering phenomena in that locale. Hereafter, we call the latter contributions the 'intrinsic' DW resistivity. Precise extraction of the intrinsic DWR can be achieved by averaging the measured longitudinal resistances, $\langle R \rangle = \left(R_{xx}^{U} + R_{xx}^{D}\right)/2$, which compensates the obfuscating contributions from the transverse voltages[24]. In Fig. 2d we plot both $\langle R(t) \rangle$, this average of experimental data, and $R^0(t) = \rho^0(t)L/A$, a simple, idealized prediction for the longitudinal resistance. Here $R^0(t)$ and $\rho^0(t)$ describe respectively the resistance and resistivity distribution along the channel; L and A are respectively the length and cross-sectional area of the channel. For the simplest example, a device containing a single DW oriented perpendicular to the channel walls, we can write $\rho^0(x(t)) = (1 - x/L)\rho_{xx}^{(i)} + (x/L)\rho_{xx}^{(f)}$. Here we assume the DW is positioned at $0 \leq x(t) \leq L$. $\rho_{xx}^{(i)}$ and $\rho_{xx}^{(f)}$ represent the asymptotic resistivities of the initial and final magnetization states, respectively; their values differ slightly (Fig. 2b). As the DW traverses the 'measurement region' between longitudinal probes, $R^0(t)$ evolves linearly, reflecting the changing fractional contributions from the two domains present. The non-zero difference between the experimental trace, $\langle R(t) \rangle$, and the simple average, $R^0(t)$, clearly displays the presence of effects beyond those associated with a simple resistivity discontinuity at the DW.

There are two fundamental contributions to this difference; we call them the 'eddy-like' and 'intrinsic' DW resistivities. The former originates from local, static variations in current density induced by the resistivity discontinuity across the DW[3,24]. (Since these contributions persist for zero DW velocity, they are distinct from true eddy currents associated with DW motion.) These eddy-like currents are only found to be appreciable when the DW is in close proximity to the probes; when the DW is roughly mid-way between these probes, $\langle R \rangle$ settles to reflect the simple linear evolution expected for $R^0(t)$ (ref. 24). However, in this 'intermediate' regime we observe a small, but distinct, negative offset from the expected value for $R^0(t)$. This offset evidently reflects the true, intrinsic contribution to the resistivity arising from an individual DW. In the intermediate regime, $x \approx L/2$, this particular device reproducibly manifests a negative offset $\langle R(x) \rangle - R^0(x) \approx -0.44\,\Omega$. This is well within our measurement resolution (~0.2 Ω), but comparable to the accuracy of our interpolation yielding $R^0(t)$ (which we estimate to be 100 p.p.m. of $\langle R \rangle$, that is, ~0.5 Ω).

To obtain further confirmation of this negative intrinsic DW resistivity, we have refined our methodology to enhance our measurement resolution (to ~10 p.p.m. of the longitudinal resistance) and to minimize extraneous contributions from the bulk magnetoresistance (Methods). First, we achieve precise alignment of the devices with respect to [110] orientation to strongly suppress contributions from the anisotropic magnetoresistance (AMR). The detailed procedure is illustrated in Fig. 3. Second, instead of measuring the DW quasistatically, as in our initial measurements, we make measurements on individual, stationary DWs at zero applied field. To accomplish this we precisely position individual DWs along the device channel in a stepwise manner, using in-plane magnetic field pulses. Between these pulses we record longitudinal resistance across the stationary DW in the absence of an applied field. These zero-field measurements upon a static DW are free of effects from the field-induced longitudinal magnetoresistance, the Lorentz-force-induced component of transverse resistance, and effects from (true) eddy currents and fluctuations that can arise from DW motion.

For these high-resolution measurements, we pattern two families of long, second-generation devices (see Methods). In Fig. 4a,b we demonstrate how DW position is precisely ascertained as it is stepped along the device (see also Methods). Figure 4a displays the evolution of the transverse resistance for the left and right pair of probes from a 30-μm-wide device.

After each step in the DW's position, we measure the longitudinal resistances R_{xx}^{U} and R_{xx}^{D} using long integration times to obtain resolution $\delta R \approx 0.1\,\Omega$ ($\delta R/\langle R \rangle \approx 5 \times 10^{-6}$). Figure 4c shows the measured longitudinal resistances R_{xx}^{U} and R_{xx}^{D}. These data traces, together with their average $\langle R \rangle$ are in good agreement with the theoretical predictions[24]. A magnified plot of $\langle R \rangle$ is displayed in Fig. 4d. For these devices, an extended phase of linear evolution is manifested in the intermediate regime, where the DW is localized between the transverse probe pairs.

Successive experiments on several devices, involving many repeated launching of individual DWs, establish firm bounds on the magnitude of this consistently negative DW resistivity. Figure 4e displays a histogram of intrinsic DWRs from 27 consecutive runs upon a precisely oriented 30-μm-wide device, taken over the course of one week. The average DWR obtained is $R_{\mathrm{DW}} \approx -1.0 \pm 0.2\,\Omega$. Two factors appear to contribute to observed variance. First, the DW orientation evidently changes slightly from run-to-run, varying between 90 ± 20°, and therefore the length of DW changes proportionately. Second, drifts in the electronics occur over the 3-hour

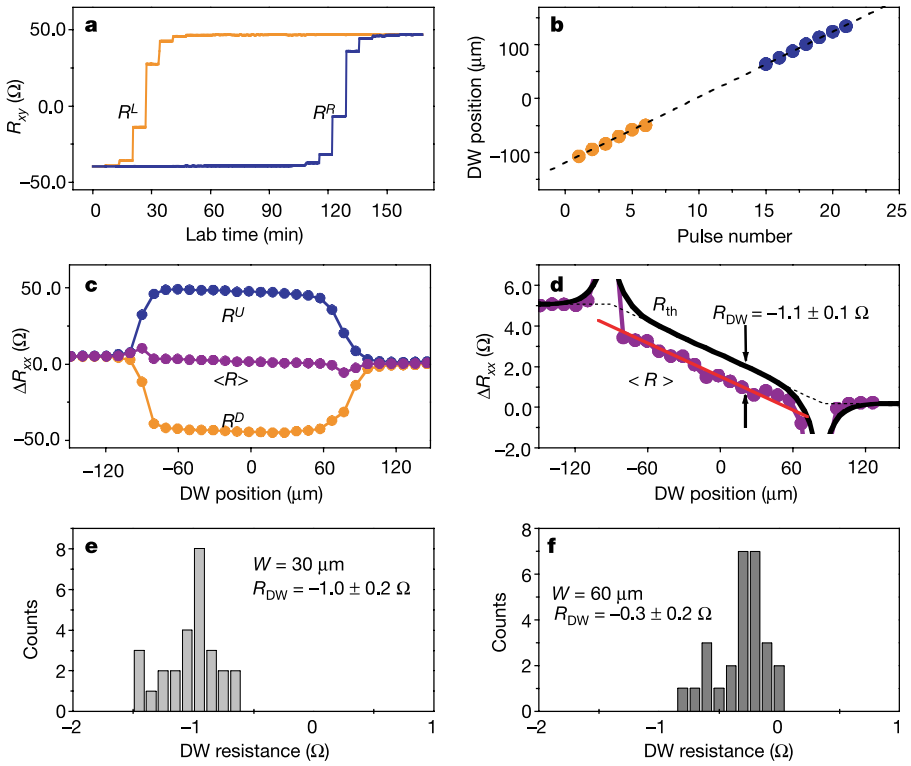

Figure 4 High-resolution extraction of the intrinsic DWR. **a**, Transverse resistance signal showing the sequential stepping of a single DW along the device channel. **b**, Calculated position of the DW as it approaches the left- and right-most pair of probes; extrapolation provides high-confidence positional data in between. **c**, Measured longitudinal resistances, R^U_{xx} (blue) and R^D_{xx} (orange), and their average, $\langle R \rangle$ (violet). The longitudinal axis is rescaled to reflect DW position and an average background resistance $R_{xx} \approx 16.8\,\mathrm{k}\Omega$ has been subtracted from all traces. **d**, Magnified view of the average resistance data (violet). The difference between the theoretical model, R^0 (black trace) and the average of data in the linear region (red line) is the DWR, $R_{DW} = -1.1 \pm 0.1\,\Omega$ for this particular experiment. **e**, **f**, Variance of the intrinsic DWR for a large number (>25) of such experiments in which single DWs are launched and stepped along two well-aligned devices (widths, $W = 30\,\mu\mathrm{m}$ and $60\,\mu\mathrm{m}$).

measurement interval, which is required to slowly and sequentially step-and-measure each nucleated DW through a given device. Figure 4f displays measurement results on a 60-μm-wide device, for which the intrinsic contribution to the DWR is found to be $R_{DW} \approx -0.3 \pm 0.2\,\Omega$. Assuming a DW width that we estimate to be $\delta_W \approx 10\,\mathrm{nm}$ (ref. 25, $T_c = 45\,\mathrm{K}$ is used in the calculations), these DWRs may be translated into effective DW resistivities: $\rho_{DW}(30\,\mu\mathrm{m}) = -(3 \pm 0.6) \times 10^{-4}\,\Omega\,\mathrm{m}$ and $\rho_{DW}(60\,\mu\mathrm{m}) = -(1.8 \pm 1.2) \times 10^{-4}\,\Omega\,\mathrm{m}$. These are quite appreciable—comparable, in fact, to the bulk resistivity of the epilayer itself, ρ. Our initial measurements (Fig. 2) yielded $\rho_{DW}(100\,\mu\mathrm{m})/\rho = -108 \pm 123\%$ for 150-nm-thick (Ga,Mn)As devices. Negative intrinsic DWR is confirmed by our subsequent high-resolution measurements on 100-nm-thick devices (Fig. 4), which yield $\rho_{DW}(30\,\mu\mathrm{m})/\rho = -100 \pm 20\%$ and $\rho_{DW}(60\,\mu\mathrm{m})/\rho = -60 \pm 40\%$.

At present, understanding of DWR is unsettled—a conflicting body of work, both experimental and theoretical, exists in the literature. DWR has, most typically, been inferred from the excess resistance arising from large ensembles of DWs within a sample[9–11]. Progress in domain imaging and nanofabrication has more recently enabled resistance measurements on samples containing significantly reduced numbers of DWs[12–15]. To date, however, the experimental results obtained from these various methods are conflicting; both positive[9,11,12,14,15] and negative[10,13] DWRs are reported. Theory has elucidated several scattering mechanisms that can yield positive DWR: reflection of carriers by the DW[4], a 'zigzag' current redistribution inside the wall due to the Hall effect[3], and spin-dependent scattering analogous to the GMR effect in magnetic multilayers[5,6]. The possibility of negative DWR arising from electronic coherence in ferromagnetic metals has also been proposed[7]. In theory, this can arise from suppression of dephasing of weakly localized electrons at a DW, thereby effectively reducing the intrinsic resistivity of DWs. Additionally, a semiclassical model, which can theoretically yield either positive or negative DWR, has been developed[8]. In this latter model, a large impurity-scattering asymmetry is required to yield a negative value.

Semiclassical models cannot account for the relatively large negative magnitude of the intrinsic DWR we observe. Although these negative DWRs could originate from quantum corrections, it is difficult to quantify the degree to which transport is phase coherent in experiments (such as these) involving ferromagnetic semiconductors. Extraction of this information from experimental data is far from straightforward; further developments in theory are clearly necessary. We anticipate that the technique for manipulating and measuring DWs reported here may be useful in ferromagnetic semiconductor devices for magnetic logic and memory[16]. These methods may also provide a new avenue for measuring quantum signatures of DW motion at low temperatures, where macroscopic quantum tunnelling of DWs should be manifested. □

Methods

Multiterminal device fabrication and magnetoresistance measurements

Our device fabrication begins with growth of 150-nm-thick $Ga_{0.948}Mn_{0.052}As$ epilayers on top of an insulating GaAs buffer layer by low-temperature molecular beam epitaxy (MBE). These epilayers are subsequently patterned into multiterminal devices, with longitudinal axes of the device channels (direction of current flow) oriented collinear with a cleave edge [110], which is also a cubic hard axis. Additional fabrication details are presented elsewhere[19,26].

Figure 1a displays the measurement set-up, showing utilization of three pairs of transverse (Hall) voltage probes to sense the magnetoresistance to a current flowing

longitudinally within the device. Measurements are carried out with a battery-supplied, constant a.c. sensing current of ≤500 nA; this is well below the onset of current-induced non-equilibrium effects. The induced transverse voltages are coupled through electrically isolated, low-noise differential amplifiers to a set of commonly synchronized lock-in amplifiers, which enable simultaneous acquisition of three signal channels. Both longitudinal and transverse resistances are recorded. The device is maintained at liquid helium temperature, while a magnetic field is applied within the epilayer plane via a precisely controlled, three-axis superconducting magnet. Magnetoresistance is obtained with a field oriented 15° away from [110] and ramped at a rate of 15 Oe s^{-1}.

Launching of individual DWs

We first apply a strong in-plane magnetic field to saturate the magnetization, then linearly ramp to a specific field magnitude with orientation anti-aligned to the initial saturation field (for example, close to the switching field labelled as point A in Fig. 1b). At ~4 K, DW nucleation then occurs infrequently through stochastic processes. Once nucleated, the constant in-plane field drives growth of the particular domain possessing magnetization most closely aligned with the applied field. We find that DW motion induced in this manner always involves propagation from a wide current contact pad into the channel. With this protocol, completely reproducible signals are detected.

High-resolution magnetoresistance measurements on single, stationary DWs

In the initial measurements, DWR was measured quasistatically as single DWs were sequentially driven slowly through the device. We have developed optimized techniques enabling high-resolution measurements on individual, stationary DWs. To accomplish this we have perfected a method allowing us to stepwise translate and position individual DWs along the device channel, through sequential, pulsed application of the in-plane magnetic field. Quick removal of the external field allows the DW to be 'frozen' at any desired location within the channel and, thereafter, the DW remains stationary for as long as we have been willing to measure. Subsequent application of in-plane field pulses allows the DW to be precisely stepped, in arbitrarily small increments, along the device channel. Between the applications of field pulses we are able to record longitudinal resistance across the stationary DW at zero applied field.

An individual DW is 'stepped' sequentially through the device, and its position is ascertained as follows. A magnetic field pulse—of magnitude 110 Oe, orientation 30° from hard axis [110], and duration 10 s—is applied every 8 min. For a given transverse-probe pair, a jump in transverse resistance is observed after each pulse, if the DW is proximal. Thereafter, the resistance remains unchanged until the next field pulse is applied. This giant planar Hall resistance allows direct computation of the DW's relative displacement from the transverse probes. Figure 4b displays the deduced positions of a DW when it is in the vicinity of the left and right pair of probes. This linear evolution of DW position confirms that the DW travels a constant, fixed distance in response to each field pulse—about 10 μm for the aforementioned conditions. For measurement points in the intermediate region, which may be 'far' from either transverse-probe pair, DW position can be reliably determined by linear extrapolation between known positions.

To enhance our ability to resolve the intrinsic DW resistivity, we minimize the longitudinal resistance background by precise alignment of the devices with respect to [110] orientation (to within ~0.03°). This is achieved through a novel protocol based upon iterative, wafer-scale electron beam lithography (Fig. 3) that permits suppression of the AMR to a value as small as $\sim \Delta R/R = 6 \times 10^{-5}$. Two families of precisely aligned devices, with widths 30 μm and 60 μm and a constant 6:1 aspect ratio (that is, length/width) from a thinner (Ga,Mn)As epilayer (100 nm thickness, Curie temperature $T_C \approx 45$ K) have been iteratively patterned. The long 6:1 aspect ratio serves to extend the intermediate region that is unperturbed by eddy-like contributions (compare Fig. 2d). To preclude spurious DW trapping along the channel itself, transverse probes are located solely at the entrance and exit of each channel (Fig. 3c).

Received 3 April; accepted 2 July 2004; doi:10.1038/nature02809.

1. Hubert, A. & Schäfer, R. *Magnetic Domains: The Analysis of Magnetic Microstructures* (Springer, Berlin, 1998).
2. Ferré, J. Dynamics of magnetization reversal: From continuous to patterned ferromagnetic films. *Topics Appl. Phys.* **83,** 127–165 (2002).
3. Berger, L. Low-field magnetoresistance and domain drag in ferromagnets. *J. Appl. Phys.* **49,** 2156–2161 (1978).
4. Cabrera, G. G. & Falicov, L. M. Theory of residual resistivity of Bloch walls. *Phys. Status Solidi B* **61,** 539–549 (1974); **62,** 217–222 (1974).
5. Viret, M. *et al.* Spin scattering in ferromagnetic thin films. *Phys. Rev. B* **53,** 8464–8468 (1996).
6. Levy, P. M. & Zhang, S. Resistivity due to domain wall scattering. *Phys. Rev. Lett.* **79,** 5110–5113 (1997).
7. Tatara, G. & Fukumura, H. Resistivity due to a domain wall in ferromagnetic metal. *Phys. Rev. Lett.* **78,** 3773–3776 (1997).
8. van Gorkom, R. P., Brataas, A. & Bauer, G. E. W. Negative domain wall resistance in ferromagnets. *Phys. Rev. Lett.* **83,** 4401–4404 (1999).
9. Viret, M. *et al.* Anisotropy of domain wall resistance. *Phys. Rev. Lett.* **85,** 3962–3965 (2000).
10. Ruediger, U., Yu, J., Zhang, S., Kent, A. D. & Parkin, S. S. P. Negative domain wall contribution to the resistivity of microfabricated Fe wires. *Phys. Rev. Lett.* **80,** 5639–5642 (1998).
11. Klein, L. *et al.* Domain wall resistivity in $SrRuO_3$. *Phys. Rev. Lett.* **84,** 6090–6093 (2000).
12. Ebels, U., Radulescu, A., Henry, Y., Piraux, L. & Ounadjela, K. Spin accumulation and domain wall magnetoresistance in 35 nm Co wires. *Phys. Rev. Lett.* **84,** 983–986 (2000).
13. Taniyama, T., Nakatani, I., Namikawa, T. & Yamazaki, Y. Resistivity due to domain walls in Co zigzag wires. *Phys. Rev. Lett.* **82,** 2780–2783 (1999).
14. Xu, Y. B. *et al.* Magnetoresistance of a domain wall at a submicron junction. *Phys. Rev. B* **61,** R14901–R14904 (2000).
15. Danneau, R. *et al.* Individual domain wall resistance in submicron ferromagnetic structures. *Phys. Rev. Lett.* **88,** 157201–157204 (2002).
16. Allwood, D. A. *et al.* Submicrometer ferromagnetic NOT gate and shift register. *Science* **296,** 2003–2006 (2002).
17. Ono, T. *et al.* Propagation of a magnetic domain wall in a submicrometer magnetic wire. *Science* **284,** 468–470 (1999).
18. Wolf, S. A. *et al.* Spintronics: A spin-based electronics vision for the future. *Science* **294,** 1488–1495 (2001).
19. Tang, H. X., Kawakami, R. K., Awschalom, D. D. & Roukes, M. L. Giant planar Hall effect in epitaxial (Ga,Mn)As devices. *Phys. Rev. Lett.* **90,** 107201–107204 (2003).
20. Ohno, H. Making nonmagnetic semiconductors ferromagnetic. *Science* **281,** 951–956 (1998).
21. Yamanouchi, M., Chiba, D., Matsukura, F. & Ohno, H. Current-induced domain-wall switching in a ferromagnetic semiconductor structure. *Nature* **428,** 539–542 (2004).
22. Welp, U., Vlasko-Vlasov, V. K., Liu, X., Furdyna, J. K. & Wojtowicz, T. Magnetic domain structure and magnetic anisotropy in $Ga_{1-x}MnAs$. *Phys. Rev. Lett.* **90,** 167206–167209 (2003).
23. Tang, H. X., Kawakami, R. K., Awschalom, D. D., Roukes, M. L.. *Phys. Rev. Lett.* (submitted).
24. Tang, H. X. & Roukes, M. L. Electrical transport across an individual magnetic domain wall in (Ga,Mn)As microdevices. *Phys. Rev. B* (submitted); preprint at ⟨http://arxiv.org/cond-mat/0403547⟩ (2004).
25. Potashnik, S. J. *et al.* Saturated ferromagnetism and magnetization deficit in optimally annealed $Ga_{1-x}MnxAs$ epilayers. *Phys. Rev. B* **66,** 012408 (2002).
26. Tang, H. X.. *Semiconductor Magnetoelectronics for Spintronics and Suspended 2DEG for Mechanoelectronics* PhD dissertation, California Inst. Technol. (2002).

Acknowledgements We acknowledge support from DARPA/DSO and AFOSR. We thank A.H. MacDonald for discussions.

Competing interests statement The authors declare that they have no competing financial interests.

Correspondence and requests for materials should be addressed to M.L.R. (roukes@caltech.edu).

Decline of surface temperature and salinity in the western tropical Pacific Ocean in the Holocene epoch

Lowell Stott[1], Kevin Cannariato[1], Robert Thunell[2], Gerald H. Haug[3], Athanasios Koutavas[4] & Steve Lund[1]

[1]*Department of Earth Sciences, University of Southern California, Los Angeles, California 90089, USA*
[2]*Department of Geological Sciences, University of South Carolina, Columbia, South Carolina 29205, USA*
[3]*Geoforschungszentrum Potsdam, D-14473 Potsdam, Germany*
[4]*Department of Earth, Atmospheric, and Planetary Sciences, Massachusetts Institute of Technology, 77 Massachusetts Avenue, Cambridge, Massachusetts 02139, USA*

In the present-day climate, surface water salinities are low in the western tropical Pacific Ocean and increase towards the eastern part of the basin[1]. The salinity of surface waters in the tropical Pacific Ocean is thought to be controlled by a combination of atmospheric convection, precipitation, evaporation and ocean dynamics[2], and on interannual timescales significant variability is associated with the El Niño/Southern Oscillation cycles. However, little is known about the variability of the coupled ocean–atmosphere system on timescales of centuries to millennia. Here we combine oxygen isotope and Mg/Ca data from foraminifers retrieved from three sediment cores in the western tropical Pacific Ocean to reconstruct Holocene sea surface temperatures and salinities in the region. We find a decrease in sea surface temperatures of ~0.5 °C over the past 10,000 yr, whereas sea surface salinities decreased by ~1.5 practical salinity units. Our data imply either that the Pacific basin as a whole has become progressively less salty or that the present salinity gradient along the Equator has developed relatively recently.

On interannual timescales, the El Niño/Southern Oscillation (ENSO) causes large changes in salinity over the equatorial Pacific as the warm, low-salinity waters from the western tropical